Journal of Systems Engineering and Electronics
Vol. 35, No. 1, February 2024, pp.14 – 23

Scale effect removal and range migration correction for hypersonic target coherent detection

WU Shang, SUN Zhi*, JIANG Xingtao, ZHANG Haonan,
DENG Jiangyun, LI Xiaolong, and CUI Guolong

School of Information and Communication Engineering, University of Electronic Science and Technology of China, Chengdu 611731, China

Abstract: The detection of hypersonic targets usually confronts range migration (RM) issue before coherent integration (CI). The traditional methods aiming at correcting RM to obtain CI mainly considers the narrow-band radar condition. However, with the increasing requirement of far-range detection, the time bandwidth product, which is corresponding to radar's mean power, should be promoted in actual application. Thus, the echo signal generates the scale effect (SE) at large time bandwidth product situation, influencing the intra and inter pulse integration performance. To eliminate SE and correct RM, this paper proposes an effective algorithm, i.e., scaled location rotation transform (ScLRT). The ScLRT can remove SE to obtain the matching pulse compression (PC) as well as correct RM to complete CI via the location rotation transform, being implemented by seeking the actual rotation angle. Compared to the traditional coherent detection algorithms, ScLRT can address the SE problem to achieve better detection/estimation capabilities. At last, this paper gives several simulations to assess the viability of ScLRT.

Keywords: hypersonic target detection, coherent integration (CI), scale effect (SE) removal, range migration (RM) correction, scaled location rotation transform (ScLRT).

DOI: 10.23919/JSEE.2023.000151

1. Introduction

The hypersonic target detection draws considerable attention and lots of research appeared [1−3]. The hypersonic target often shows features including ultra-fast speed, low-observability and far-range flight, causing signal to noise ratio (SNR) reduction [4,5]. As a widely applicable technique, the long-time coherent integration (CI) is able to heighten echo SNR effectively [6,7]. Unfortunately, the range migration (RM) may appear within the large coherent interval [8−10]. The traditional CI methods which can correct the RM are appropriate for the narrow-band radar [11,12]. However, with the enhancement of radar transmitting power and improvement of range resolution, the time bandwidth product of radar should be increased and the conventional narrow-band condition will be no longer valid in practical situation [13,14]. Within the large time bandwidth product situation, the conventional pulse compression (PC) might confront the mismatching problem, including sinc envelope deformation and sinc envelop off-centering. And all these mismatch effects are collectively called as the scale effect (SE) [15,16]. The SE will bring about serious SNR degradation within the process of intra pulse integration when still using the traditional CI methods and then the performance of inter pulse integration (i.e., the CI) may also be influenced, which will finally affect detection/estimation capacities. Therefore, the elimination for SE and RM effects should be conducted before CI.

So far, the majority of researching output with respect to the CI only takes into account of the RM problem. The moving target detection (MTD) could achieve the CI by Doppler filter bank to accomplish inter pulse coherent superposition to promote the echo's SNR [17,18]. Unfortunately, the MTD could not correct the RM [19]. The Radon Fourier transform (RFT) seeks the echo trajectory and obtains CI in the range-velocity domain [20−22]. The improved axis rotation-MTD (IAR-MTD) corrects RM by axis rotation and obtains CI by slow time Fourier transform (FT) [23]. The scaled inverse Fourier transform (SCIFT) could execute the symmetric autocorrelation transform to eliminate RM, which increases noise level and affects the CI result [24]. Generally, these fore-

Manuscript received December 23, 2022.
*Corresponding author.
This work was supported by the National Natural Science Foundation of China (62101099), the Chinese Postdoctoral Science Foundation (2021M690558; 2022T150100; 2018M633352; 2019T120825), the Young Elite Scientist Sponsorship Program (YESS20200082), the Aeronautical Science Foundation of China (2022Z017080001), the Open Foundation of Science and Technology on Electronic Information Control Laboratory, and the Natural Science Foundation of Sichuan Province (2023NSFSC1386).

going CI algorithms are unable to remove SE and encounter detection capability reduction.

To remove SE and achieve the coherent detection results for the large time bandwidth product radar, Qian, et al. put forward a modified RFT called wideband scaled RFT (WSRFT) [15]. Xu et al. proposed a high-resolution accumulation algorithm aiming at solving SE for high-speed platform in [16]. However, these algorithms may lose efficacy for the situation when the velocity cannot be obtained.

On the basis of [5], this paper completes SE removal and RM correction and extends the content in [5]. This paper mathematically analyzes both the intra pulse and inter pulse motions for hypersonic target. To remove SE and correct RM as well as completing the coherent detection, we propose a novel method, i.e., scaled location rotation transform (ScLRT). The ScLRT can jointly realize PC and CI by seeking echo rotation angle. Comparing to conventional CI algorithms, the ScLRT can efficaciously eliminate SE to obtain excellent detection/estimation performance. Eventually, several numerical simulations are performed to evaluate the ScLRT's availability.

The detailed content in this paper is arranged as follows. In Section 2, the hypersonic target echo is modeled containing intra and inter pulse movement is built. Then, Section 3 introduces ScLRT detailedly. The simulated trails are performed in Section 4 to evaluate the viability and efficacy of ScLRT. Finally, Section 5 makes a conclusion for this paper.

2. Signal modeling

Suppose the radar antennas emits the linear frequency modulated signal:

$$s_{\text{emit}}(t_n,t)=\text{rect}\left(\frac{t}{T_p}\right)\exp\left(\text{j}\pi\psi t^2\right)\cdot \exp\left[\text{j}2\pi f_c(t_n+t)\right] \tag{1}$$

where $t_n=nT_r$ denotes the slow time, n and T_r separately represent the pulse number and pulse repetition interval, t denotes intra pulse sampling time (i.e., fast time), and T_p, ψ and f_c severally indicate the pulse duration, frequency modulated rate and carrier frequency.

Assume that a hypersonic target moves at the velocity of v, as shown in Fig. 1. Concurrently taking into account the intra and inter pulse motion, we can see precede the nth pulse is transmitted, the target has already flown for $t+t_n$. After moving for single pass time-delay δ, the nth pulse catches up the target. Thus, we can achieve the following equation:

$$\frac{\text{c}\delta}{2}=R_0+V(t+t_n)+\frac{v\delta}{2} \tag{2}$$

where $V(\cdot)$ denotes the radial velocity, c indicates the light speed, and R_0 represents the initial range.

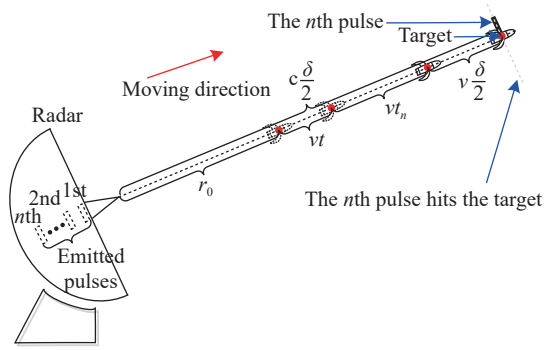

Fig. 1 Motion diagram

Based on (2), the instantaneous slant range could be written as

$$R(t,t_n)=R_0+v(t+t_n). \tag{3}$$

Therefore, we can obtain the expression of δ:

$$\delta=\frac{2R(t,t_n)}{\text{c}-v}. \tag{4}$$

Then, the demodulated echo is able to be given as

$$s_{\text{echo}}(t_n,t)=\rho_0\text{rect}\left(\frac{t-\delta}{T_p}\right)\exp\left[\text{j}\pi\psi(t-\delta)^2\right]\cdot \exp\left(-\text{j}2\pi f_c\delta\right) \tag{5}$$

where ρ_0 denotes the echo complex amplitude.

Assume range variable R corresponds to the fast time t, then we have $t=2R/(\text{c}-3v)$. Since the sample frequency could be given as $f_s=mB$ (where m indicates the sample ratio and $m=2$ in this paper), we can obtain $R=d_rk$ and $R_0=d_rk_0$, where $d_r=\text{c}/(2f_s)$ denotes the range cell, k and k_0 denote range cell numbers corresponding to R and R_0, respectively. Therefore, the fast time can be given as $\delta=2d_rk/(\text{c}-3v)$. It should be pointed out that the slow time could be written as $t_n=nT$. Then, substituting (3) and (4) into (5), we can obtain the demodulated echo:

$$s_{\text{echo}}(n,k)=\rho_0\text{rect}\left[\frac{\varsigma}{T_p}\left(\frac{2d_rk}{\text{c}-3v}-\delta_n\right)\right]\cdot \exp\left[\text{j}\pi\psi\varsigma^2\left(\frac{2d_rk}{\text{c}-3v}-\delta_n\right)^2\right]\cdot \exp\left(-\text{j}\pi\varpi\frac{4d_rk}{\text{c}-3v}\right)\exp\left(-\text{j}2\pi f_c\varsigma\delta_n\right) \tag{6}$$

where $\varsigma=(\text{c}-3v)/(\text{c}-v)$ denotes the scale coefficient, $\delta_n=2(d_rk_0+vnT)/(\text{c}-3v)$ is the time-delay, and $\varpi=2vf_c/(\text{c}-v)$.

Performing the FT on the fast time (i.e., $2d_rk/(\text{c}-3v)$) for (6), we can get the frequency echo [25] as follows:

$$S_{\text{echo}}(n,f)=\rho_1\text{rect}\left(\frac{f+\varpi}{\varsigma B_1}\right)\exp\left(-\text{j}\pi\frac{f^2}{\psi\varsigma^2}\right)\cdot$$
$$\exp\left[\text{j}2\pi f\left(-\frac{\gamma}{\psi\varsigma^2}-\delta_n\right)\right]\cdot$$
$$\exp\left(-\text{j}4\pi f_c\frac{d_r k_0+\nu nT}{\text{c}-3\nu}\right)\exp\left(-\text{j}\pi\frac{\varpi^2}{\psi\varsigma^2}\right) \tag{7}$$

where f indicates the range frequency variable that corresponds with $2d_r k/(\text{c}-3\nu)$ (i.e., the fast time), $B_1=\psi T_p$ indicates the signal bandwidth, and ρ_1 is the FT complex amplitude.

Using the conventional matched filter, i.e., $M(f)=\text{rect}(f/B_1)\exp(\text{j}\pi f^2/\psi)$, to complete range direction PC [12,14,26−30]:

$$s_{\text{mpc}}(n,k)=\underset{f}{\text{IFT}}(S_{\text{echo}}(n,f)\cdot M(f))=$$
$$\int_{-\infty}^{+\infty}\rho_2\text{rect}\left(\frac{f+\frac{\varpi}{2}+\frac{\nu B_1}{2(\text{c}-\nu)}}{B_1-\varpi-\frac{\nu B_1}{\text{c}-\nu}}\right)\cdot$$
$$\exp\left[\text{j}\pi\frac{f^2}{\psi}\left(1-\frac{1}{\varsigma^2}\right)\right]\cdot\exp\left(-\text{j}2\pi\frac{f\varpi}{\psi\varsigma^2}\right)\cdot$$
$$\exp(-\text{j}2\pi f\delta_n)\exp\left(\text{j}\pi f\frac{4d_r k}{\text{c}-3\nu}\right)\text{d}f \tag{8}$$

where $\underset{f}{\text{IFT}}(\cdot)=\int_{-\infty}^{+\infty}(\cdot)\exp\left(\text{j}\pi f\frac{4d_r k}{\text{c}-3\nu}\right)\text{d}f$ is the inverse FT (IFT). $\rho_2=\rho_1\exp(-\text{j}\pi\varpi^2/\psi\varsigma^2)\exp(-\text{j}2\pi f_c\delta_n)$.

By analyzing (8), we can see that the first two exponential terms will lead to SE. Particularly, we have the following two conclusions:

(i) $\exp\left[\text{j}\pi\frac{f^2}{\psi}\left(1-\frac{1}{\varsigma^2}\right)\right]$ makes the sinc envelope out of shape, including the peak dropping and the main-lobe broadening in the time domain.

(ii) $\exp\left(-\text{j}2\pi\frac{f\varpi}{\psi\varsigma^2}\right)$ results in the sinc envelope center shifting.

Therefore, these two exponential terms must be removed, otherwise the SE appears and affects the intra pulse integration result.

When $1/\varsigma^2\simeq 1$, the SE will disappear and the ideal PC is capable of being achieved as

$$s_{\text{ipc}}(n,k)\simeq\rho_3\text{sinc}\left[\frac{\pi}{m}\left(k-k_0-\frac{\nu nT}{d_r}\right)\right]\cdot$$
$$\exp\left[\frac{-\text{j}4\pi f_c d_r}{\text{c}}\left(k_0+\frac{\nu nT}{d_r}\right)\right] \tag{9}$$

where ρ_3 denotes the complex amplitude of ideal PC result. From (9), we can see the ideal PC result has the standard sinc envelope in the time domain because the secondary phase and envelope of the matched filter (MF) are accurately matched with those of the frequency echo signal.

To evaluate the influence of SE, a simulation example comparing the ideal PC and conventional PC is provided as follows.

Example 1 Suppose a hypersonic target flies with the movement as: initial range cell $R_0=200$ and target's velocity $\nu=3\,000$ m/s. Table 1 provides the radar parameters. The ideal PC and conventional PC results of individual pulse are given in Fig. 2. Particularly, Fig. 2(a) shows that when the SE appears, the sinc envelope of the single pulse suffers from peak descent and main-lobe broadening as well as the center shifting after the conventional PC. For the sake of quantitatively analyzing the influence of SE, the results in dB form are also given in Fig. 2(b). Apparently, the conventional PC result confronts about a 10.55 dB SNR loss in comparison with the ideal PC, which is caused by SE.

Table 1 Radar simulated parameters

Radar parameter	Value
Carrier frequency/GHz	1.5
Bandwidth/MHz	200
Sample frequency/MHz	400
Pulse repetition frequency/Hz	500
Pulse duration/ms	1.8
Number of pulses	250

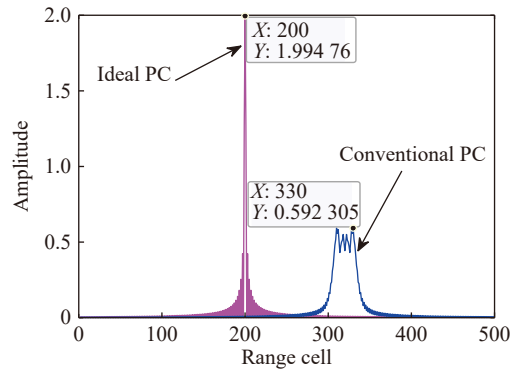

(a) Ideal PC and conventional PC results

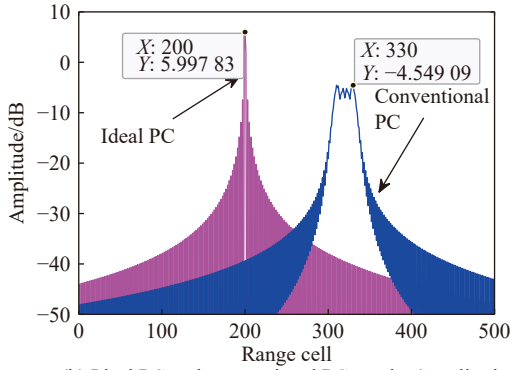

(b) Ideal PC and conventional PC results (amplitude in dB form)

Fig. 2 Ideal PC and conventional PC comparison

3. Coherent detection via ScLRT

As shown in Fig. 3, the relation between v and the intersection angle ϕ can be given as $v = d_r \tan\phi / T$. Multiply with (7) and perform

$$S_{\text{echo}}(n,f) = \rho_1 \text{rect}\left(\frac{f+\varpi_\phi}{\varsigma_\phi B_1}\right)\exp\left(-\text{j}\pi\frac{f^2}{\psi\varsigma_\phi^2}\right)\cdot \exp\left[\text{j}2\pi f\left(-\frac{\varpi_\phi}{\psi\varsigma_\phi^2}-\delta_{\phi n}\right)\right]\exp(-\text{j}2\pi f_c\delta_{\phi n})\cdot \exp\left(-\text{j}\pi\frac{\varpi_\phi^2}{\psi\varsigma_\phi^2}\right) \tag{10}$$

where $\varsigma_\phi = (\text{c}-3d_r\tan\phi/T)/(\text{c}-d_r\tan\phi/T)$ is the scale coefficient corresponding to ϕ. $\varpi_\phi = 2d_r\tan\phi f_c/[T(\text{c}-d_r\tan\phi/T)]$ and $\delta_{\phi n} = 2(d_r k_0 + d_r\tan\phi n)/(\text{c}-3d_r\cdot\tan\phi/T)$.

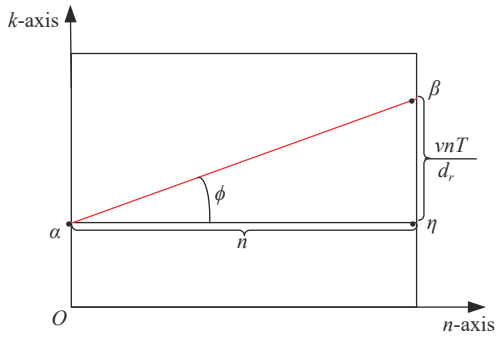

Fig. 3 Diagram illustrating the relation between v and ϕ

In general, the proposed method includes two main sequential procedures, i.e., matching PC, and RM correction and CI.

3.1 Matching PC

The matching PC needs searching rotation angle to realize intra pulse accumulation. Establishing MF at first, which corresponds to the searching angle ϕ', can be indicated as

$$M_1(f;\phi') = \text{rect}\left(\frac{f+\varpi'_\phi}{\varsigma'_\phi B_1}\right)\exp\left(\text{j}\pi\frac{f^2}{\psi\varsigma'^2_\phi}\right)\cdot \exp\left(\text{j}2\pi\frac{f\varpi'_\phi}{\psi\varsigma'^2_\phi}\right)\exp\left(\text{j}\pi\frac{\varpi'^2_\phi}{\psi\varsigma'^2_\phi}\right) \tag{11}$$

where $\varsigma'_\phi = (\text{c}-3d_r\tan\phi'/T)/(\text{c}-d_r\tan\phi'/T)$ and $\varpi'_\phi = 2d_r\cdot\tan\phi' f_c/[T(\text{c}-d_r\tan\phi'/T)]$.

Multiplying (11) with (10) and performing the IFT, we have

$$s_{\text{pc}}(n,k;\phi') = \underset{f}{\text{IFT}}(S_{\text{echo}}(n,f)\cdot M_1(f;\phi')) = \int_{-\infty}^{+\infty}\rho_1\text{rect}\left(\frac{f+\varpi_\phi}{\varsigma_\phi B_1}\right)\text{rect}\left(\frac{f+\varpi'_\phi}{\varsigma'_\phi B_1}\right)\cdot \exp\left[-\text{j}\pi\frac{f^2}{\psi}\left(\frac{1}{\varsigma_\phi^2}-\frac{1}{\varsigma'^2_\phi}\right)\right]\exp\left[-\text{j}2\pi\frac{f}{\psi}\left(\frac{\varpi_\phi}{\varsigma_\phi^2}-\frac{\varpi'_\phi}{\varsigma'^2_\phi}\right)\right]\cdot \exp\left[\frac{-\text{j}\pi}{\psi}\left(\frac{\varpi_\phi^2}{\varsigma_\phi^2}-\frac{\varpi'^2_\phi}{\varsigma'^2_\phi}\right)\right]\exp[-\text{j}2\pi(f+f_c)\delta_{\phi n}]\cdot \exp\left(\text{j}\pi f\frac{4d_r k}{\text{c}-3d_r\tan\phi/T}\right)\text{d}f. \tag{12}$$

If the searching rotation angle satisfies $\phi' = \phi$, the PC result will obtain the peak value. Meanwhile, we have $\varsigma'_\phi = \varsigma_\phi$ as well as $\delta'_\phi = \delta_\phi$ and the matching PC result is achieved as

$$s_{\text{pc}}(n,k) = \rho_4\text{sinc}\left[\frac{\pi\text{c}}{m(\text{c}-d_r\tan\phi/T)}(k-k_0-n\tan\phi)\right]\cdot \exp\left(\frac{-\text{j}4\pi f_c d_r k_0}{\text{c}-3d_r\tan\phi/T}\right)\cdot\exp\left(-\text{j}4\pi d_r f_c\frac{n\tan\phi}{\text{c}-3d_r\tan\phi/T}\right) \tag{13}$$

where ρ_4 denotes the complex amplitude after PC.

We can find that the peak of (13) changes with n, which means the RM still exists in the PC result for the hypersonic target.

3.2 RM correction and CI

The RM elimination diagram is illustrated in Fig. 4. Initially, target's energy trajectory is distributed along $\alpha\beta$. That is, the actual intersection angle is ϕ ($\angle\beta\alpha\eta$). As for the last pulse at $\beta(n,k)$, if we have $\phi' \neq \phi$, the proposed rotation method will shift this pulse from β to γ. At the moment, the energy trajectory becomes $\alpha\gamma$. Then, the RM is incompletely eliminated. If $\phi' = \phi$, the last pulse is situated at η and the RM is eliminated.

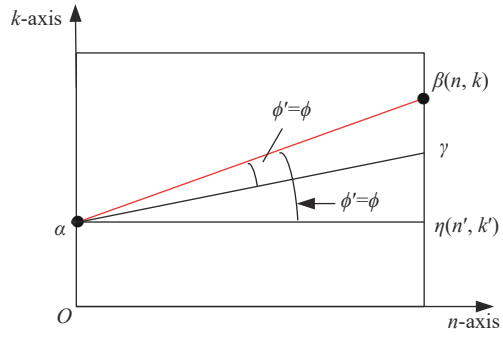

Fig. 4 Diagram for location rotation transform

The relation between (n,k) and (n',k') can be given as follows:

$$\begin{cases} n = n' \\ k = n'\tan\phi' + k' \end{cases}. \tag{14}$$

Substitute (14) into (13) and we can get

$$s_{\mathrm{pc}}(n',k';\phi')=\rho_4\mathrm{sinc}\left\{\frac{\pi \mathrm{c}}{m(\mathrm{c}-d_r\tan\phi/T)}[(k'-k_0)+n'(\tan\phi'-\tan\phi)]\right\}\exp\left(\frac{-\mathrm{j}4\pi f_c d_r k_0}{\mathrm{c}-3d_r\tan\phi/T}\right)\cdot\exp\left(-\mathrm{j}4\pi d_r f_c\frac{n'\tan\phi}{\mathrm{c}-3d_r\tan\phi/T}\right). \tag{15}$$

When $\phi'=\phi$, $n'(\tan\phi'-\tan\phi)$ in the sinc term of (15) is equivalent to zero. At this time, the RM is corrected and the CI of multi-pulses reach to the peak value. Then, the rotation angle can be calculated as

$$\hat{\phi}=\arg\max_{\phi'}\left|\underset{n'T}{\mathrm{FT}}(s_{\mathrm{pc}}(n',k';\phi'))\right| \tag{16}$$

where $\underset{n'T}{\mathrm{FT}}(\mathrm{g})$ denotes the Fourier transform with respect to $n'T$.

$$\hat{v}=\frac{d_r\tan\hat{\phi}}{T} \tag{17}$$

After correcting the RM, (15) can be given as

$$s_{\mathrm{pc}}(n',k')=\rho_4\mathrm{sinc}\left[\frac{\pi \mathrm{c}}{m(\mathrm{c}-d_r\tan\phi/T)}(k'-k_0)\right]\cdot\exp\left(\frac{-\mathrm{j}4\pi f_c d_r k_0}{\mathrm{c}-3d_r\sin\phi/T}\right)\cdot\exp\left(-\mathrm{j}4\pi d_r f_c\frac{n'\tan\phi}{\mathrm{c}-3d_r\tan\phi/T}\right)=\rho_4\mathrm{sinc}\left[\frac{\pi c}{m(\mathrm{c}-v)}(k'-k_0)\right]\exp\left(\frac{-\mathrm{j}4\pi f_c d_r k_0}{\mathrm{c}-3v}\right)\cdot\exp\left(-\mathrm{j}4\pi f_c\frac{vn'T}{\mathrm{c}-3v}\right). \tag{18}$$

Executing FT on $n'T$ to complete CI, namely

$$s_{\mathrm{CI}}(f_{n'T},k')=\rho_6\mathrm{sinc}\left[\frac{\pi \mathrm{c}}{m(\mathrm{c}-v)}(k'-k_0)\right]\cdot\mathrm{sinc}\left[T_N\left(f_{n'T}+\frac{2Vf_c}{\mathrm{c}-3v}\right)\right] \tag{19}$$

where $\rho_6=\rho_5\exp\left(\frac{-\mathrm{j}4\pi f_c d_r k_0}{\mathrm{c}-3v}\right)$, ρ_5 denotes the FT complex amplitude along the slow time, $T_N=NT$ is the coherent processing interval, N represents total pulse number, and $f_{n'T}$ denotes the Doppler frequency corresponding to $n'T$.

In (19), the CI result is achieved and the detection is realized via constant false alarm rate (CFAR).

Next, a simulated example is given to discuss the influence of SE for CI results of ScLRT and RFT.

Example 2 A hypersonic target is added in the simulation scene. The target parameters are set as: the initial range cell $R_0=400$ and target's velocity $v=3\,000$ m/s. Here, using the parameters of Table 1 and Fig. 5 shows the comparison results. Specifically, the rotation angle searching result is given in Fig. 5(a), where the searched angle is about 86.42°. By using the searched angle, the matching PC and RM correction is implemented in Fig. 5(b) and Fig. 5(c), severally. Whereafter, Fig. 5(d) indicates the CI of ScLRT, which has the peak value 479.1. The conventional PC result of RFT is displayed in Fig. 5(e). Contrasting the magnified figures in Fig. 5(b)−Fig. 5(e), we can find due to eliminating SE, ScLRT has superior PC performance than RFT. Then, RFT has the CI amplitude of 128.8, as exhibited in Fig. 5(f). In addition, Fig. 5(d) and Fig. 5(f) illustrate that the CI envelop of RFT becomes not a sinc shape mainly because of SE. Therefore, the ScLRT has better CI capability than RFT because it can both eliminate SE and RM.

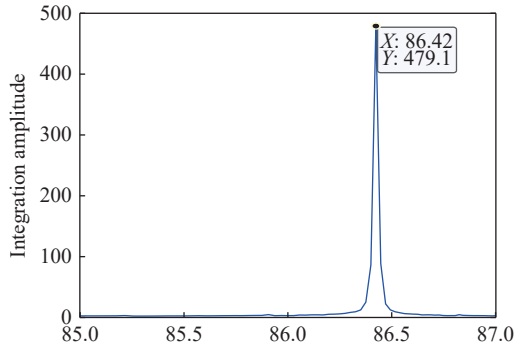

(a) Searching result of the rotation angle via ScLRT

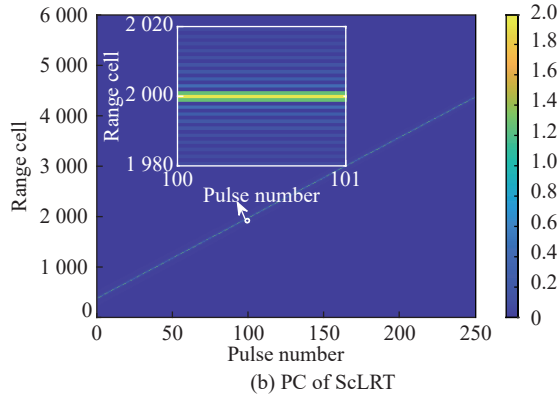

(b) PC of ScLRT

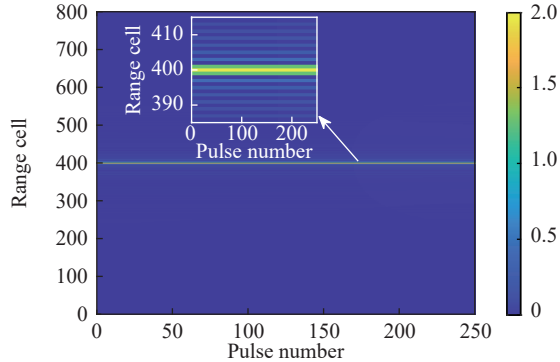

(c) RM correction of ScLRT

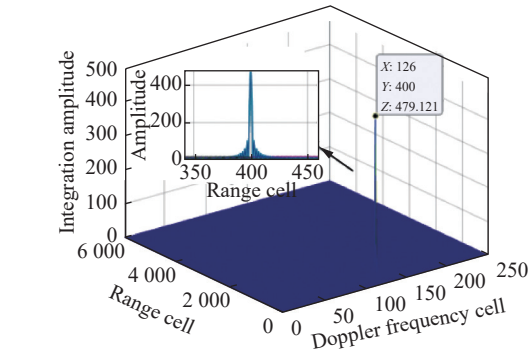

(d) CI of ScLRT

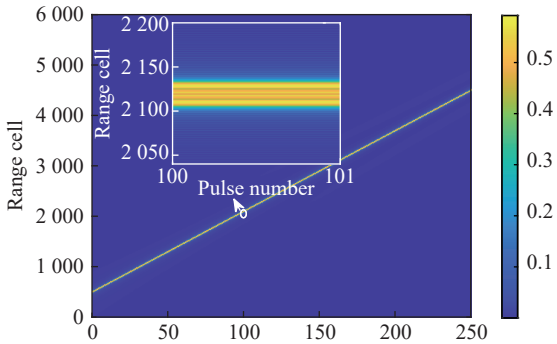

(e) PC of RFT

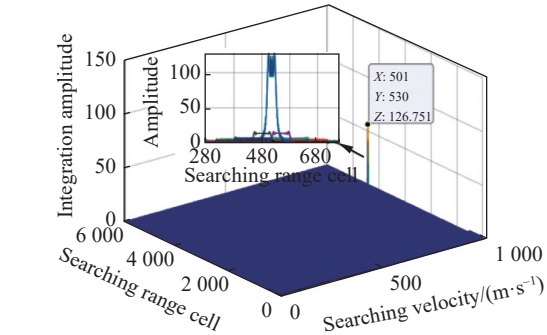

(f) CI of RFT

Fig. 5 CI comparisons of ScLRT and RFT

The flow diagram of ScLRT is given in Fig. 6 and the detailed realization steps could be summarized as follows:

Step 1 Transmitting an linear frequency modulation (LFM) signal which is given in (1) and achieving the echo signal after the demodulation in (5).

Step 2 Applying FT along the range direction with respect to (5). Then, we could achieve (7).

Step 3 Expressing (7) as (10) by variable substitution and initializing the searching region of the rotation angle.

Step 4 Constructing the matched filter as expressed in (11), which corresponds to the searching angle.

Step 5 Traversing all the searching angles to successively realize PC and location rotation transform (as given in (14)) and the searched angle could be confirmed via the peak value, which is presented in (16).

Step 6 Using the searched angle to realize the matching PC and correct RM. After RM correction, CI can be obtained in (19).

Step 7 Performing the CFAR detection via the accumulation output in (19). Specifically, contrasting the CI peak amplitude (namely test statistic) to the self-adapting threshold under a certain false alarm probability, which can be stated as

$$|s_{\mathrm{CI}}(f_{n'T},k')|>\chi \tag{20}$$

where χ indicates the level of the threshold, decided by the CI's reference unit. When (20) can be satisfied, the target is able to be detected.

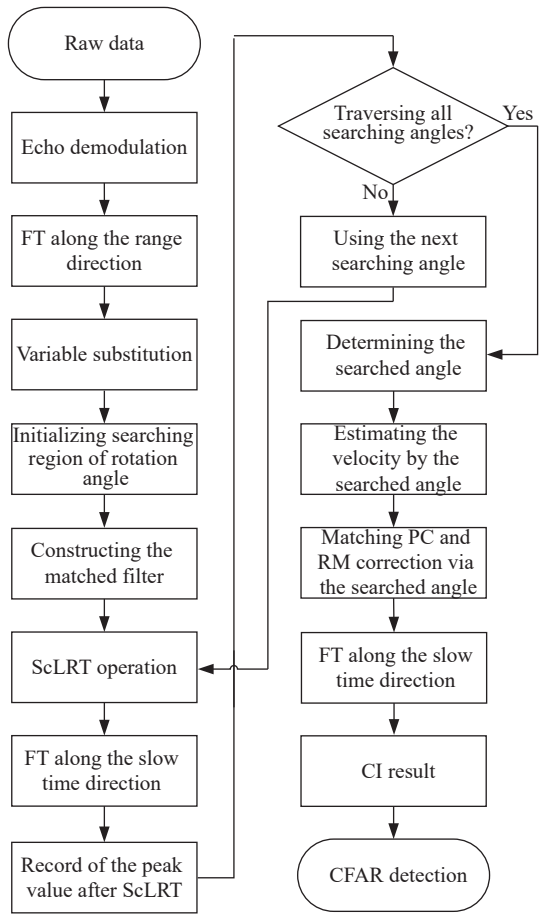

Fig. 6 Flow diagram of ScLRT

3.3 Remark

Differing from the keystone transform-based or RFT-based methods [31], the ScLRT can effectively avoid the

influence of Doppler ambiguity, mainly because the RM is corrected via rotating the intersection angle ϕ, as shown in Fig. 4. The intersection angle is just relative to the actual velocity, instead of the ambiguity velocity [9]. Therefore, the RM correction result of ScLRT only depends on whether the echo trajectory can be completely rotated by searching the intersection angle.

4. Numerical simulations

This section evaluates the presented method of different performance according to simulated trails, which include CI, input-output SNR, detection and velocity estimation. The radar and movement simulated parameters are exactly the same as those in Example 2. Furthermore, typical CI algorithms are also given to be compared with the proposed ScLRT algorithm, including RFT, IAR-MTD, SCIFT, and MTD.

4.1 CI performance

The CI of RFT, IAR-MTD, SCIFT, MTD, and ScLRT are contrasted. The SNR before PC is −49 dB and Fig. 7 exhibits the CI results. To be specific, the CI of ScLRT is provided in Fig. 7(a) and its peak value is about 418.2. Fig. 7(b) gives the CI of RFT with the peak value of 128.2. The CI of IAR-MTD with the peak value of about 126 is shown in Fig. 7(c). Apparently, the CI of RFT and IAR-MTD are inferior to the ScLRT's because of SE. Fig. 7(d) provides the CI of SCIFT, where the target is submerged and hard to be detected due to the raised noise level after symmetric autocorrelation. Furthermore, the SE also has some effects on CI of SCIFT. Moreover, the CI of MTD is given in Fig. 7(e) and it suffers from the problems of SE and RM but cannot address them. Thus, the MTD also becomes invalid in its CI output. Totally, the ScLRT obtains superior CI performance than any other compared method.

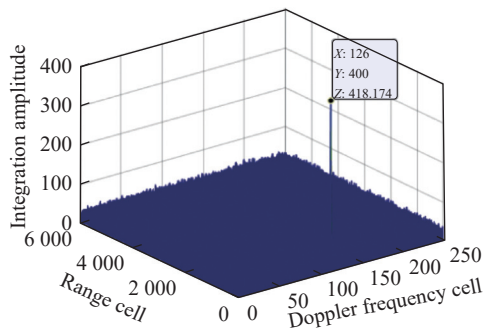

(a) ScLRT CI output

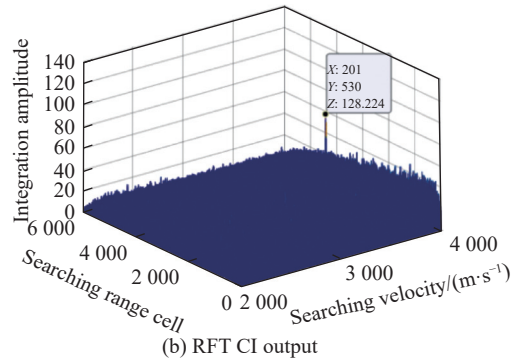

(b) RFT CI output

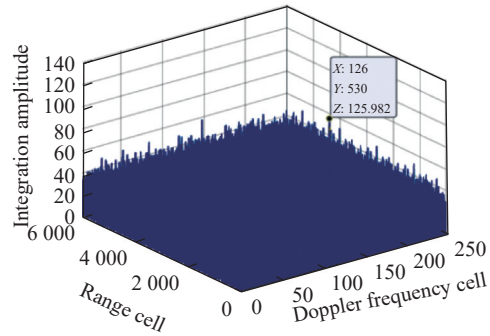

(c) IAR-MTD CI output

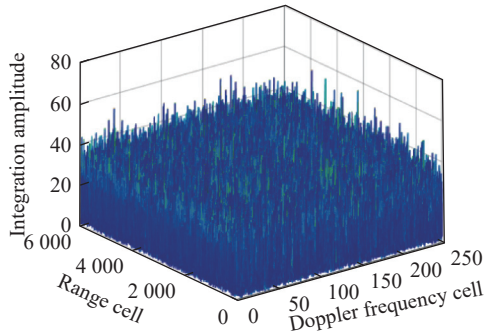

(d) SCIFT CI output

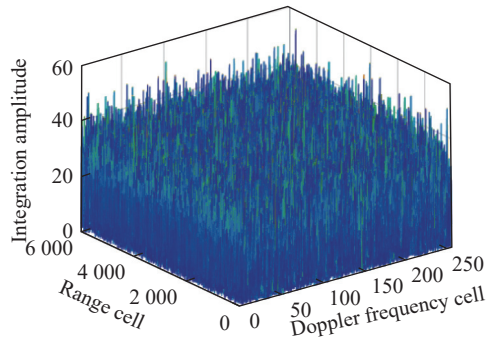

(e) MTD CI output

Fig. 7 CI performance comparison

4.2 Input-output SNR performance

The results of the input-output SNR performance for several typical methods (i.e., RFT, IAR-MTD, and SCIFT) and the ScLRT are given in Fig. 8. The region of input

SNR are set as [−85 dB, −35 dB] and 500 Monte Carlo experiments are executed for each SNR-in value. In Fig. 8, the result of the ideal MTD is also shown. Comparing the input-output SNR capability of the RFT to ScLRT's, the RFT-based method suffers from 7 dB loss. As for the input-output SNR capability, ScLRT exceeds IAR-MTD (8 dB) and SCIFT (14 dB).

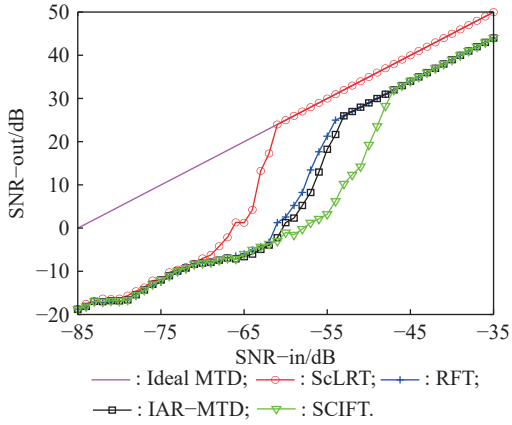

Fig. 8 Input-output SNR performance

4.3 Detection performance

This section compares the detection performance of ScLRT and the representative algorithms (i.e., MTD, SCIFT, IAR-MTD, and RFT) are analyzed by the Monte Carlo trails with the probability of false alarm as 10^{-4} [6]. The SNR regions are [−75 dB, −25 dB]. Fig. 9 provides the detection results of the above mentioned five algorithms after performing 500 Monte Carlo trials for each SNR. From Fig. 9, we can see ScLRT possesses better detection performance than RFT, IAR-MTD, and SCIFT, because the ScLRT can jointly eliminate the SE and RM. Furthermore, the MTD has the worst detection result in all the five methods since it can neither remove the SE nor correct the RM.

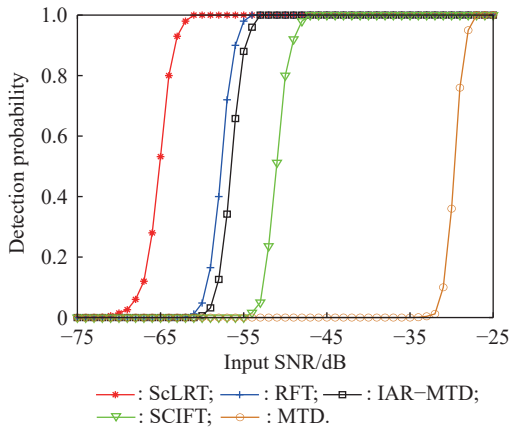

Fig. 9 Detection performance

4.4 Velocity estimation performance

This section gives the velocity estimation performance results for ScLRT and several typical methods, including RFT, IAR-MTD, and SCIFT. Note that the region of the SNR variation is set as [−75 dB, −40 dB] and 500 Monte Carlo operations are applied for each given SNR. Fig. 10 gives the velocity estimation results, where the ScLRT can obtain the best velocity estimation performance among the four methods. In particular, the RFT, IAR-MTD, and SCIFT respectively suffer from 7 dB, 8 dB, and 14 dB performance loss for the root-mean square error (RMSE) of target's velocity because of SE, comparing to the proposed algorithm.

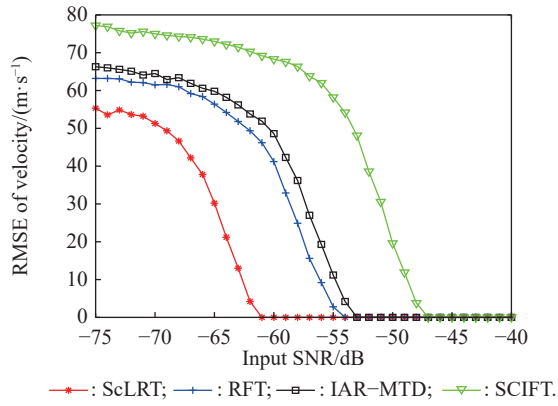

Fig. 10 Velocity estimation performance

5. Conclusions

This paper models the echo of hypersonic target considering intra pulse and inter pulse movements firstly, where SE will appear for the large time bandwidth product radar. Then, the ScLRT has been proposed to remove SE and correct RM with two successive procedures of matching PC and CI by seeking rotation angle. Comparing with the typical CI methods, the proposed one can obtain superior performance of CI, input-output SNR, target detection and velocity estimation. Numerical simulated trails have proved the viability and efficacy of the ScLRT method.

In the future, we will focus on the unmanned aerial vehicle swarm detection [32,33], fast CI implementation by segmentation [34], and clutter situation [35−37].

References

[1] LI L, WANG G H, SUN D X, et al. A hypersonic target coherent integration detection algorithm based on Doppler feedback. Journal of Systems Engineering and Electronics, 2020, 31(1): 85–94.

[2] SU J, XING M D, WANG G, et al. High-speed multi-target detection with narrowband radar. IET Radar, Sonar and Navi-

gation, 2010, 4(4): 595–603.
[3] CHEN X L, GUAN J, LIU N B, et al. Maneuvering target detection via Radon fractional Fourier transform based long-time coherent integration. IEEE Trans. on Signal Processing, 2014, 62(4): 939–953.
[4] LI X L, CUI G L, YI W, et al. Polynomial Radon polynomial Fourier transform for near space hypersonic maneuvering target detection. IEEE Trans. on Aerospace and Electronic Systems, 2018, 54(3): 1306–1322.
[5] WU S, SUN Z, JIANG X T, et al. A coherent integration method for high-speed target via scale effect elimination and across range unit correction. Proc. of the 7th International Conference on Signal and Image Processing, 2022: 787−791.
[6] HUANG P H, LIAO G S, WANG Z W, et al. Long-time coherent integration for weak maneuvering target detection and high-order motion parameter estimation based on keystone transform. IEEE Trans. on Signal Processing, 2016, 15: 4013–4026.
[7] TIAN J, CUI W, WU S L. A novel method for parameter estimation of space moving targets. IEEE Geoscience and Remote Sensing Letters, 2014, 11(2): 389–393.
[8] XING M D, SU J H, WANG G Y, et al. New parameter estimation and detection algorithm for high speed small target. IEEE Trans. on Aerospace and Electronic Systems, 2011, 47(1): 214–224.
[9] SUN Z, LI X L, YI W, et al. A coherent detection and velocity estimation algorithm for the high-speed target based on the modified location rotation transform. IEEE Journal of Selected Topics in Applied Earth Observation and Remote Sensing, 2018, 11(7): 2346–2361.
[10] SUN Z, LI X L, YI W, et al. Detection of weak maneuvering target based on Keystone transform and matched filtering process. Signal Processing, 2017, 140: 127–138.
[11] HUANG P H, LIAO G S, YANG Z W, et al. An approach for refocusing of ground moving target without target motion parameter estimation. IEEE Trans. on Geoscience and Remote Sensing, 2017, 55(1): 336–350.
[12] LI X L, CUI G L, YI W, et al. Coherent integration for maneuvering target detection based on Radon-Lv's distribution. IEEE Signal Processing Letters, 2015, 22(9): 1467–1471.
[13] XU J, XIA X G, PENG S B, et al. Radar maneuvering target motion estimation based on generalized Radon-Fourier transform. IEEE Trans. on Signal Processing, 2012, 60(12): 6190–6201.
[14] SUN Z, LI X L, CUI G L, et al. A fast approach for detection and parameter estimation of maneuvering target with complex motions in coherent radar system. IEEE Trans. on Vehicular Technology, 2021, 70(10): 10278–10292.
[15] QIAN L C, XU J, XIA X G, et al. Wideband scaled Radon-Fourier transform for high-speed radar target detection. IET Radar, Sonar and Navigation, 2016, 10(9): 1671–1682.
[16] XU X F, LIAO G S, YANG Z W, et al. Moving-in-pulse duration model-based target integration method for HSV-borne high-resolution radar. Digital Signal Processing, 2017, 68: 31–43.
[17] SKOLNIK M I, LINDE G, MEADS K. Senrad: an advanced wideband air-surveillance radar. IEEE Trans. on Aerospace and Electronic Systems, 2001, 37(4): 1163–1175.
[18] SKOLNIK M I. Introduction to radar system. New York: McGraw-Hill, 2002.
[19] RAO X, TAO H H, SU J, et al. Axis rotation MTD algorithm for weak target detection. Digital Signal Processing, 2014, 26: 81–86.
[20] XU J, YU J, PENG Y N, et al. Radon-Fourier transform (RFT) for radar target detection (I): generalized Doppler filter bank processing. IEEE Trans. on Aerospace and Electronic Systems, 2011, 47(2): 1186–1202.
[21] XU J, YU J, PENG Y N, et al. Radon-Fourier transform (RFT) for radar target detection (II): blind speed sidelobe suppression. IEEE Trans. on Aerospace and Electronic Systems, 2011, 47(4): 2473–2489.
[22] YU J, XU J, PENG Y N, et al. Radon-Fourier transform (RFT) for radar target detection (III): optimality and fast implementations. IEEE Trans. on Aerospace and Electronic Systems, 2012, 48(2): 991–1004.
[23] RAO X, ZHONG T T, TAO H H, et al. Improved axis rotation MTD algorithm and its analysis. Multidimensional Systems and Signal Processing, 2019, 30: 885–902.
[24] ZHENG J B, SU T, ZHU W T, et al. Radar highspeed target detection based on the scaled inverse Fourier transform. IEEE Journal of Selected Topics in Applied Earth Observation and Remote Sensing, 2015, 8(3): 1108–1119.
[25] BAO Z, XING M D, WANG T. Radar imaging technology. Beijing: House of Electronics Industry, 2005.
[26] SUN Z, JIANG X T, ZHANG H N, et al. Joint elimination method of scale effect and range migration/Doppler migration for hypersonic maneuvering target under large time-bandwidth product condition. Signal Processing, 2023, 210: 109074.
[27] SUN Z, LI X L, CUI G L, et al. Hypersonic target detection and velocity estimation in coherent radar system based on scaled Radon Fourier transform. IEEE Trans. on Vehicular Technology, 2020, 69(6): 6525–6540.
[28] SUN Z, CHEN H X, LI X L, et al. Airborne radar coherent integration and sea-clutter suppression method for marine moving target via TSLRT-MFP-SVD. Proc. of the IEEE International Geoscience and Remote Sensing Symposium, 2022: 22091567.
[29] XIONG K, ZHAO G H, SHI G M, et al. Radar high-speed target coherent detection method based on modified Radon inverse Fourier transform. IEEE Trans. on Aerospace and Electronic Systems, 2023, 59(2): 950–962.
[30] CAO Y F, WANG W Q, ZHANG S S. Long-time coherent integration for high-order maneuvering target detection via zero-trap line extraction. IEEE Trans. on Aerospace and Electronic Systems, 2021, 57(6): 4017–4027.
[31] ZHAN M Y, HUANG P H, ZHU S Q, et al. A modified Keystone transform matched filtering method for space-moving target detection. IEEE Trans. on Geoscience and Remote Sensing, 2017, 60: 5105916.
[32] ZHENG J B, CHEN R X, YANG T Y, et al. An efficient strategy for accurate detection and localization of UAV swarms. IEEE Internet of Things Journal, 2021, 8(20): 15372–15381.
[33] ZHENG J B, YANG T Y, LIU H W, et al. Accurate detection and localization of unmanned aerial vehicle swarms-enabled mobile edge computing system. IEEE Trans. on Geoscience and Remote Sensing, 2021, 17(7): 5059–5067.
[34] CHEN H X, LI X L, WANG K Y, et al. Computational efficient segmented integration method for high-speed maneuvering target detection. Signal Processing, 2022, 195:

108475.
[35] SUN Z, CHEN H X, JIANG X T, et al. SMLRT-GRT-SVD based sea-surface slow and small target signal integration and clutter suppression method for airborne radar. Journal of Signal Processing, 2022, 38(7): 1380–1391. (in Chinese)
[36] GUO Q, CHEN J T, QI L G, et al. Sea clutter suppression algorithm based on improved singular value decomposition. Journal of Xidian University, 2023, 50(2): 188–196. (in Chinese)
[37] CHEN M, WAN X R, ZHAN W J, et al. Micro-Doppler clutter suppression based on sparsity adaptive matching pursuit algorithm. Journal of Terahertz Science and Electronic Information Technology, 2023, 21(6): 830–837. (in Chinese)

Biographies

WU Shang was born in 1991. He received his B.S degree from Nanjing University of Aeronautics and Astronautics in 2013, and M.S. degree from National University of Defense Technology in 2015. He is a Ph.D. candidate in University of Electronic Science and Technology of China. His research interests are radar high-speed target detection and multiple-input and multiple-output (MIMO) radar detection.
E-mail: 18612784412@163.com

SUN Zhi was born in 1992. He received his B.S. degree from Zhengzhou University, Zhengzhou, China, and Ph.D. degree in signal and information processing from the University of Electronic Science and Technology of China (UESTC), Chengdu, China, in 2015 and 2020, respectively. He is an associate researcher with the School of Information and Communication Engineering, UESTC. From March 2019 to March 2020, he was a visiting Ph.D. with the School of Electrical and Electronic Engineering, Nanyang Technological University, Singapore, under the financial support from the China Scholarship Council (CSC). His research interests include weak target detection, time-frequency analysis, and clutter suppression.
E-mail: zhisunuestc@163.com

JIANG Xingtao was born in 1999. He received his B.S. degree from North China Electric Power University, Baoding, China. He is working toward his M.S. degree in the School of Information and Communication Engineering, University of Electronic Science and Technology of China, Chengdu, China. His research interests include moving target detection and airborne radar clutter suppression.
E-mail: fjxt_1999@163.com

ZHANG Haonan was born in 2000. He received his B.S. degree from North China Electric Power University, Baoding, China. He is working toward his M.S. degree in the School of Information and Communication Engineering, University of Electronic Science and Technology of China, Chengdu, China. His research interests include moving target detection and airborne radar clutter suppression.
E-mail: zhang18844908287@163.com

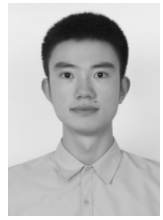

DENG Jiangyun was born in 2000. He received his B.S. degree from Jiangxi University of Science and Technology, Ganzhou, China. He is working toward his M.S. degree in the School of Information and Communication Engineering, University of Electronic Science and Technology of China, Chengdu, China. His research interests include weak target detection and multiple-input and multiple-output (MIMO) radar signal processing.
E-mail: 1203513569@qq.com

LI Xiaolong was born in 1989. He received his B.S. and Ph.D. degrees from the University of Electronic Science and Technology of China (UESTC), Chengdu, China, in 2011 and 2017, respectively. Since 2017, he has been a faculty with the School of Information and Communication Engineering, UESTC. From 2018 to 2019, he was a visiting researcher with the Department of Electrical and Computer Engineering, National University of Singapore, Singapore. He is an associate professor with UESTC. His research interests include radar moving target detection, weak signal parameter estimation, and multiple-input and multiple-output (MIMO) radar signal processing.
E-mail: xiaolongli@uestc.edu.cn

CUI Guolong received his B.S., M.S., and Ph.D. degrees from the University of Electronic Science and Technology of China (UESTC), Chengdu, China, in 2005, 2008, and 2012, respectively. From January 2011 to April 2011, he was a visiting researcher with the University of Naples Federico II, Naples, Italy. From June 2012 to August 2013, he was a postdoctoral researcher with the Department of Electrical and Computer Engineering, Stevens Institute of Technology, Hoboken, NJ, USA. From September 2013 to July 2018, he was an associate professor with UESTC. Since August 2018, he has been a professor with UESTC. His current research interests include cognitive radar, array signal processing, multiple-input and multiple-output (MIMO) radar, and through the wall radar.
E-mail: cuiguolong@uestc.edu.cn